

Supplemental Material

“Coherent Force Chains in Disordered Granular Materials Emerge from a Percolation of Quasilinear Clusters”

K. P. Krishnaraj and Prabhu R. Nott

Department of Chemical Engineering, Indian Institute of Science, Bangalore 560012, India

I. Particle dynamics simulations

The Discrete Element Method (DEM) is a particle dynamics simulator with an elastoplastic interaction force, which is widely used for computational simulation of granular statics and flow [R1]. Our simulations were conducted using the open source molecular dynamics package LAMMPS [R2], and the contact model and its DEM implementation are described in Ref. [R3]. In DEM the particles are treated as deformable, and their interaction forces are calculated from the normal overlap and tangential displacement post contact. The dissipative interaction is modelled by spring-dashpot modules for the normal and tangential directions (Fig. S1), and an additional Coulomb slider in the latter to incorporate a rate-independent frictional force, an important feature of granular materials. For a pair of spheres i, j of radii R_i, R_j at positions $\mathbf{x}_i, \mathbf{x}_j$ in contact, the overlap is

$$\delta \equiv R_i + R_j - |\mathbf{x}_{ij}| \quad (\text{S1})$$

where $\mathbf{x}_{ij} \equiv \mathbf{x}_i - \mathbf{x}_j$; the particles are in contact only when the overlap is positive. The components of the relative velocity normal and tangential to the point of contact are

$$\mathbf{v}_{n_{ij}} = (\mathbf{v}_{ij} \cdot \mathbf{n}_{ij}) \mathbf{n}_{ij} \quad (\text{S2})$$

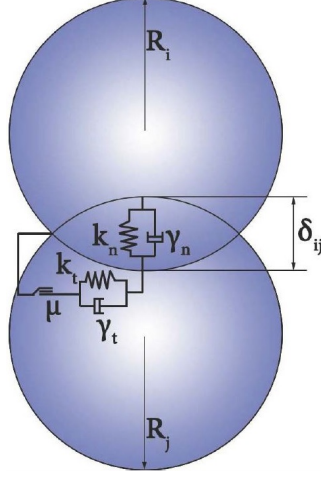
$$\mathbf{v}_{t_{ij}} = \mathbf{v}_{ij} - \mathbf{v}_{n_{ij}} - (\boldsymbol{\omega}_i R_i + \boldsymbol{\omega}_j R_j) \times \mathbf{n}_{ij} \quad (\text{S3})$$

where $\mathbf{n}_{ij} \equiv \mathbf{x}_{ij}/|\mathbf{x}_{ij}|$ is the unit normal from j to i , $\mathbf{v}_{ij} \equiv \mathbf{v}_i - \mathbf{v}_j$, and $\boldsymbol{\omega}_i, \boldsymbol{\omega}_j$ are the rotational velocities of particles i and j . The tangential spring displacement $\mathbf{u}_{t_{ij}}$ is initiated at the time of contact and can be calculated by integrating,

$$\frac{d\mathbf{u}_{t_{ij}}}{dt} = \mathbf{v}_{t_{ij}} - \frac{(\mathbf{u}_{t_{ij}} \cdot \mathbf{v}_{ij}) \mathbf{x}_{ij}}{|\mathbf{r}_{ij}^2|} \quad (\text{S4})$$

The second term represents rigid body rotation around the point of contact and ensures that $\mathbf{u}_{t_{ij}}$ lies in the tangent plane of contact.

For simplicity, the springs are assumed to be linear (Hookean). Previous studies [R3] have shown that employing non-linear springs that corresponds to Hertzian contact makes no qualitative difference. The normal and tangential forces imparted on i by j are



Parameter	Value
k_n	$1.336 \times 10^5 (m_p g / d_p)$
k_t	$\frac{2}{7} k_n$
γ_n	$87.82 (g / d_p)^{1/2}$
γ_t	$\frac{1}{2} \gamma_n$

FIG. S1. Schematic of the soft particle interaction model between spheres of radii R_i and R_j . The values of parameters used in the model are given in the table, where g is the gravitational acceleration on earth, and m_p is the mass of a particle of diameter d_p .

$$\mathbf{F}_{n_{ij}} = k_n \delta_{ij} \mathbf{n}_{ij} - \gamma_n m_{\text{eff}} \mathbf{v}_{n_{ij}} \quad (\text{S5})$$

$$\mathbf{F}_{t_{ij}} = \begin{cases} -k_t \mathbf{u}_{t_{ij}} - \gamma_t m_{\text{eff}} \mathbf{v}_{t_{ij}} & \text{if } |\mathbf{F}_{t_{ij}}| < \mu |\mathbf{F}_{n_{ij}}| \\ -\mu |\mathbf{F}_{n_{ij}}| \mathbf{v}_{t_{ij}} / |\mathbf{v}_{t_{ij}}| & \text{otherwise} \end{cases} \quad (\text{S6})$$

where k_n and k_t are the normal and tangential spring stiffness coefficients, γ_n and γ_t the corresponding damping coefficients, μ is the coefficient of friction for the Coulomb slider, and $m_{\text{eff}} \equiv m_i m_j / (m_i + m_j)$ is the effective mass of the two spheres. The velocities and positions of the particles are updated by integrating Newton's second law,

$$m_i \dot{\mathbf{v}}_i = \sum_j \mathbf{F}_{ij} + \mathbf{F}_i^{\text{ext}}, \quad I_i \dot{\boldsymbol{\omega}}_i = -\frac{\sum_j \mathbf{x}_{ij} \times \mathbf{F}_{ij}}{2} \quad (\text{S7})$$

where pairwise additivity of the interaction forces is assumed, and $\mathbf{F}_i^{\text{ext}}$ is the external force (such as gravity).

For the linear spring-dashpot-slider model, the time of contact is [40]

$$t_{\text{coll}} = \pi(2k_n/m - \gamma_n^2/4)^{-1/2}. \quad (\text{S8})$$

The choice of the normal spring stiffness coefficient determines the collision time between two particles. The simulation time step is chosen such that each collision is resolved accurately, and the choice of $\Delta t = t_{\text{coll}}/50$ is found to be sufficiently small [30,R3]. Since the collision time decreases with increasing spring stiffness k_n , it is standard practice to optimize the value of k_n such that it is large enough for the macroscopic behaviour to mimic that of hard particles, and the time step is large enough for the computations to be tractable. The parameters used in the simulations are listed in Fig. S1. The values of k_n , k_t and γ_t was chosen based on previous

studies [30,R3] that have attempted to model hard grains such as glass beads and sand. The value of γ_n chosen is such that the normal coefficient of restitution is 0.7. In all our computations, μ is set to 0.5. The 2D simulations were conducted by placing spheres in a plane and allowing movement only within the plane.

The particle sizes were chosen from a uniform distribution with lower and upper limits of $0.8d_p$ and $1.2d_p$ respectively, where d_p is the mean diameter. The walls were constructed with particles of diameter d_p set in a close packed linear (2D) or triangular (3D) lattice. In all the simulations, the constants characterizing grain-wall interactions are the same as those for grain-grain interactions.

II. Subnetwork sampling and characterization

The network of interacting particles is analyzed by considering contacts as the basic units, or nodes. The nodes are connected by edges, which physically correspond to particle triplets [Fig. S2(a-c)]. Identification of the nodes and edges transforms the network into a weighted directed graph. It is important that the graph be a directed one so that all permissible nodes are reached from a given seed node. As a result, the triplets that a contact is associated with depends on the direction chosen. For example, the set of triplets that the contact A-B in Fig. S2(a) is associated with depends on whether the contact vector is A→B or B→A. The weight of edge i - j is the triplet linearity $r_{ij} \equiv \mathbf{n}_i \cdot \mathbf{n}_j$, where \mathbf{n}_i is unit vector corresponding to node i [Fig. S2(c)].

For a particle configuration with N_c contacts and a given value of the network linearity r (as defined in Eq. 1), the $2N_c \times 2N_c$ adjacency matrix A is constructed [R4,R5], whose elements A_{ij} represent the connectivity of edges i - j [Fig. S2(d)] and are given by,

$$A_{ij} = \begin{cases} 0, & r_{ij} < r \\ 1, & r_{ij} \geq r \end{cases} \quad (\text{S9})$$

An illustration of the procedure applied to a simple representative particle configuration is shown in Fig. S2. It is easy to see that the resulting graph becomes increasingly sparse as the network linearity r increases.

The above-described transformation of the particle packing into a contact based directed graph allows the use of standard tools of graph analysis. For example, the number of contacts that can be reached from a given contact for a fixed value of linearity is estimated by standard search methods used in graphs. The commonly used methods to find reachability in graphs are the Breadth First Search (BFS) and Depth First Search (DFS) [R4,R5]. We have used the BFS method in this study. For a given value of linearity r and a seed contact, the number of edges in the subgraph can be identified. Enumeration of all the subgraphs would require repeating the search for every contact chosen as a seed, which is computationally challenging for large systems. Instead, a large enough fraction of the contacts is randomly chosen as seeds, and the task of enumeration of the subgraphs is reduced to one of sampling. Choosing 10% of all cont-

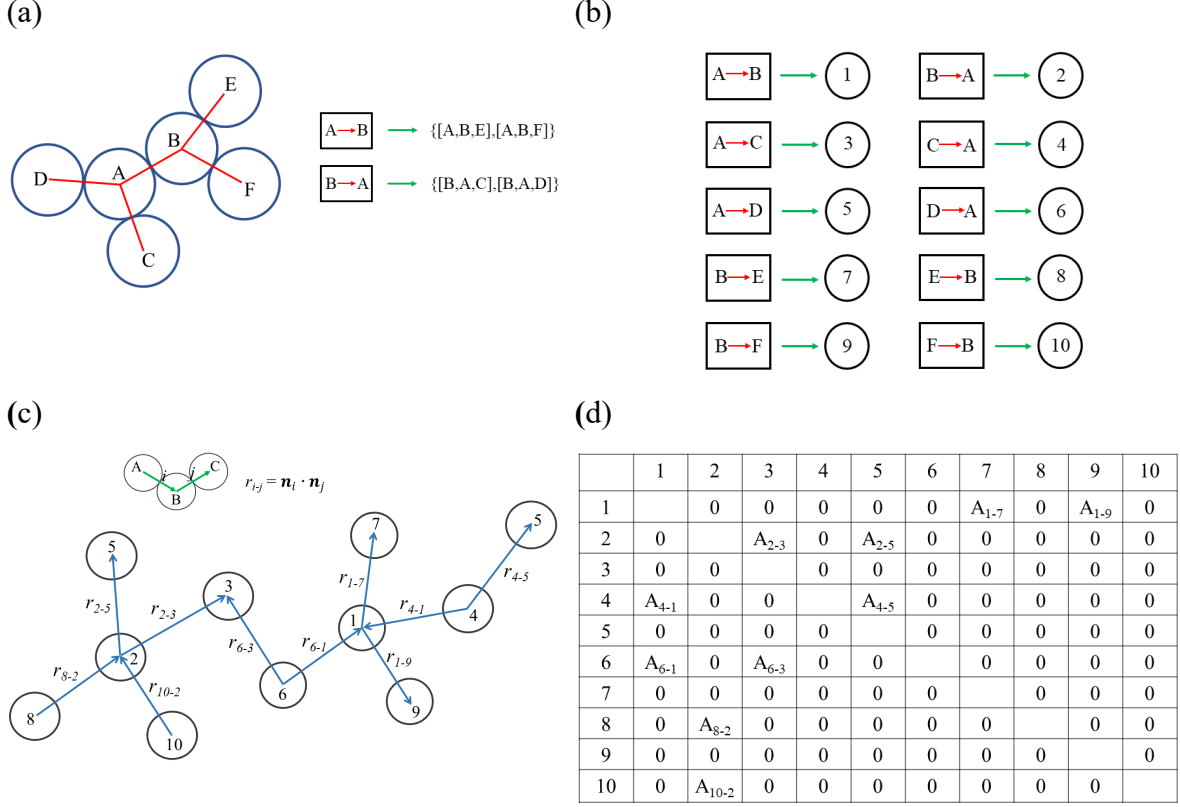


FIG. S2. The cluster identification algorithm. (a) Triplets associated with a contact: the contacts $A \rightarrow B$ and $B \rightarrow A$ are connected to different neighbouring contacts in a directed graph. (b) Each directed contact is assigned a unique identity. (c) Weighted directed graph representation of the particle packing shown in (a), we note that, triplets with $r_{ij} < 0$ are not considered. (d) The adjacency matrix representation of (c) in which the elements $A_{ij} = 1$ if the edge $i-j$ satisfies the linearity criterion $r_{ij} \geq r$, and 0 otherwise.

acts as seeds yields sufficiently accurate statistics. Increasing the percentage of seeds beyond 10% leaves the results unchanged.

A. Percolation probability and mean cluster size

The percolation probability is found from the subgraphs originating or terminating at wall particles. In isotropic compression, a subgraph is considered percolating if it spans the boundaries of at least a single dimension. In uniaxial compression and plane shear, a subgraph is considered percolating if it spans the non-periodic dimension. In silos, a subgraph is considered percolating if it spans the boundaries in the direction of gravity.

We use the standard definition of cluster number $n(s)$ as the number of subgraphs with s unique contacts. The mean cluster size $S(r)$ then is [25],

$$S(r) = \frac{\sum n_s s^2}{\sum n_s s} \quad (\text{S10})$$

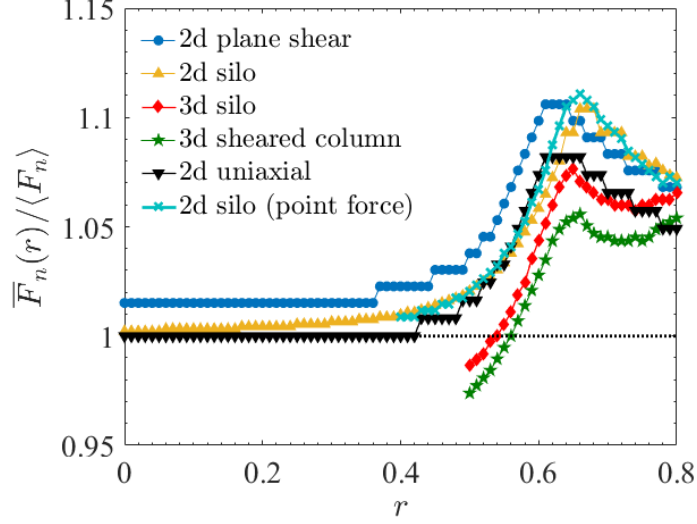


FIG. S2.1. Average cluster force as a function of linearity for anisotropic systems. The linearity r corresponding to the maximum of $\bar{F}_n(r)$ for the different systems are, 0.62 (2D plane shear), 0.67 (2D silo), 0.65 (3D silo), 0.66 (3D sheared column), 0.63 (2D uniaxial compression) and 0.66 (2D silo with point force). The results are averages over 400 configurations for the point force study and 200 configurations for the others.

where the summation is over all s . The infinite, or system-spanning, clusters are excluded from the summation.

B. Estimation of critical linearity and exponents

The value of r_c is obtained from the scaling relation,

$$r_c^{\text{eff}}(L) - r_c \propto L^{1/\nu} \quad (\text{S11})$$

where $r_c^{\text{eff}}(L)$ is the effective critical linearity of a system of size L , and ν is the correlation length exponent. The estimation of $r_c^{\text{eff}}(L)$ and critical exponents are detailed in Rintoul & Torquato [R6] and Pathak et al [21].

The error estimates of the exponents were determined from the 95% confidence interval bounds from regression analysis. The critical exponents and their confidence intervals for isotropic compression were obtained from 2000 configurations, and for random geometric graphs from 50000 configurations, see Sec. IV.

For anisotropic systems, no clear procedure exists for estimating the critical exponents. For the purpose of this paper it suffices to obtain an estimate of r_c , which we get from the maximum of average cluster force $\bar{F}_n(r)$ (Fig. S2.1). Our analysis of isotropic systems [Fig. 3(b)] suggests that this is a good approximation.

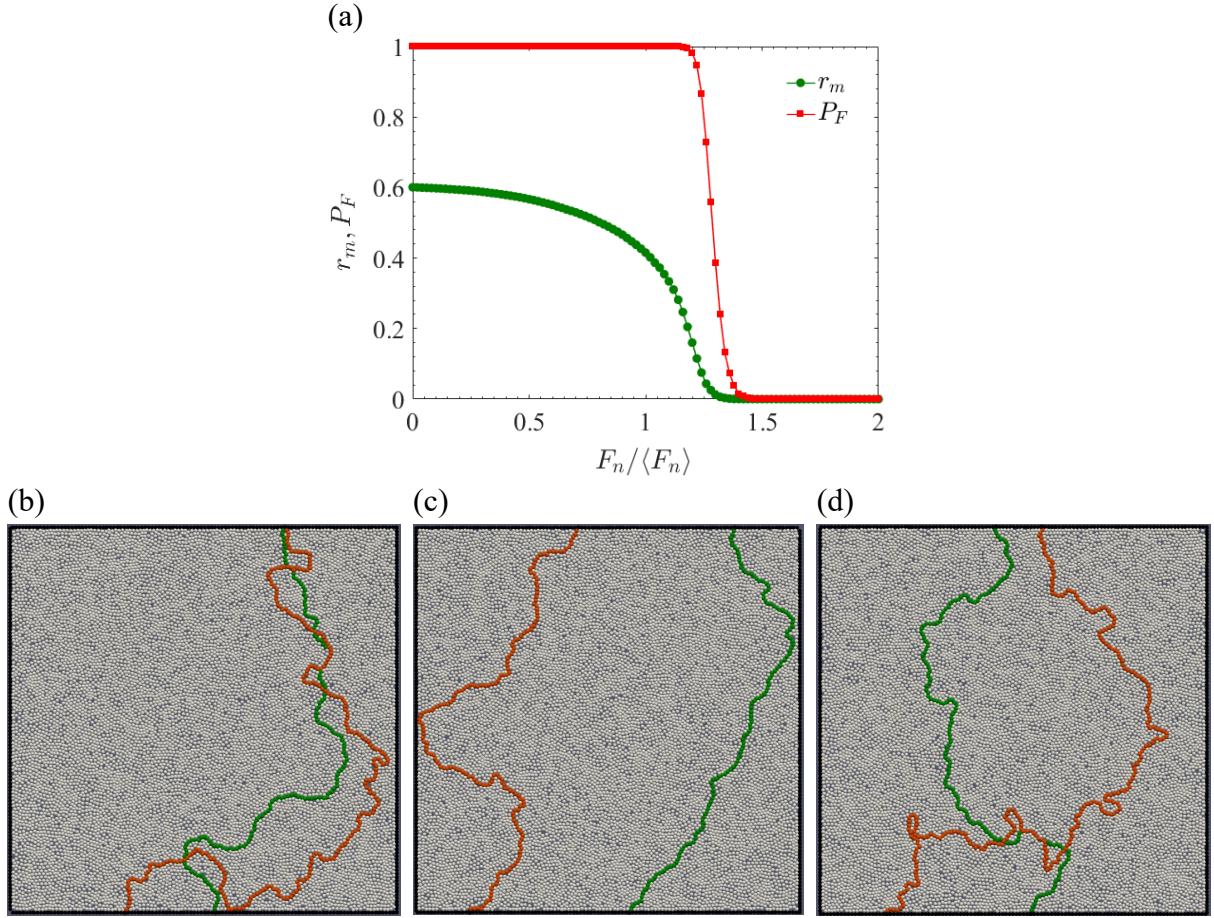


FIG. S2.2. Structural order in force cutoff based subnetworks. (a) Linearity of force percolation-based subnetworks. Also shown is the percolation probability P_F of clusters whose contacts bear a minimum force of F_n . (b-d) Three configurations showing the maximally linear force percolating paths with threshold force F_c (red) and linearity percolating paths (green): (b) $\hat{r}_c = 0.58$, $F_c = 1.20$, $r_m(F_c) = 0.08$, (c) $\hat{r}_c = 0.59$, $F_c = 1.25$ ($r_m(F_c) = 0.16$) and (d) $\hat{r}_c = 0.61$, $F_c = 1.25$ ($r_m(F_c) = 0.06$). The results are for 2D isotropic compression with dimensions $100d_p \times 100d_p$, area fraction of 0.8132. The results in (a) are averages over 2000 configurations.

C. Linearity of force percolation-based subnetworks

To show the structure of clusters obtained from force percolation, we examined the linearity of system-spanning clusters corresponding to a given force threshold F_n . As in Refs [13,21], we isolated the subnetwork of contacts carrying a normal force of F_n or higher, and determined the maximally linear system-spanning path in the subnetwork. To obtain the maximum linearity $r_m(F_n)$ of a subnetwork with force threshold F_n , we have used Dijkstra's algorithm [R4,R5,R7] with priority queues. As shown in Fig. S2.2(a), the maximal linearity of the subnetwork monotonically decreases with increasing F_n . The critical force F_n^c at which there is percolation is in the range $1.2-1.5\langle F_n \rangle$, for which the linearity $r < 0.1$. At such low linearity, the subnetwork is essentially random, and hence the subnetwork at F_n^c bears no resemblance to force chains. This inference is corroborated visually in Fig. S2.2(b-d), where we have shown

for three randomly chosen configurations the maximally linear force percolating paths with threshold F_n^c (red lines) along with linearity percolation paths (green) of linearity \hat{r}_c (which is close to, but not necessarily equal to r_c). It is clear that the force percolation paths are much more tortuous than the linearity percolating paths.

D. Orientation of clusters

The distribution of the orientation of clusters [Fig. 4(a-c)] is determined in the following manner. For a given value of linearity r , a random seed contact is chosen, and the clusters of connected to it are traced. The orientations of the vectors connecting the seed contact to every contact i in the cluster [Fig. S2.3(a)] are then determined; in two dimensions the angle θ with one coordinate axis determines the orientation. This is repeated over many seeds and multiple configurations, and the probability distribution $P_{cl}(\theta, r)$ of the orientation of such vectors is determined. $P_{cl}(\theta, r)$ is defined unambiguously if the sampling is conducted over every contact chosen as a seed; in practice, we find that randomly choosing 10% of the total number of contacts as seeds in each configuration, and averaging over a sufficiently large number of configurations, provides accurate statistics. The results shown in Fig. 4(a-c) are averages over 200 configurations.

The orientation of clusters in a gravity-bound vertical column is determined in a slightly different manner. Here, the mean orientation of clusters of linearity r connected to the walls in static and sheared vertical columns was determined by choosing contacts with wall particles as the seeds. For each wall particle j , the clusters emanating from its contacts are traced, and the angle θ_i subtended by the line connecting the wall particle with particle i in the clusters with the horizontal (in the clockwise direction) is determined [Fig. S2.3(b)]. The average orientation of clusters θ is

$$\theta = \frac{\sum_{j=1}^{N_w} \frac{1}{N_c} \sum_{i=1}^{N_c} \theta_i}{N_w} \quad (\text{S12})$$

where N_c is the number of particles in the critical clusters emanating from the wall particle j , and N_w is the number of wall particles in the vertical strip Δz connected to at least one cluster. We average over vertical bins of width $\Delta z \approx 11d_p$ and over many configurations to determine the $\theta(z)$ profiles in Fig. 4(e,f). In the sheared column, the critical cluster angles were measured along the stationary wall. The results shown in Fig. 4(e,f) are averages over 200 and 3000 configurations for the static and sheared columns, respectively.

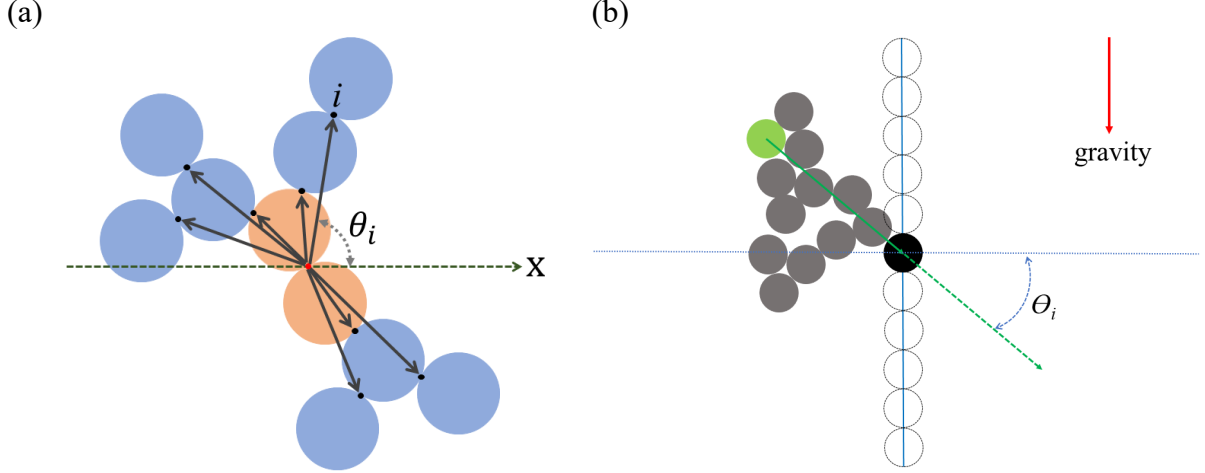


FIG. S2.3. (a) Schematic of cluster orientation estimation. For each value of the linearity r , the orientation of the vectors joining a seed contact (light brown particles) to all contacts in the cluster are measured with respect to an arbitrary coordinate axis. The orientations are collected over a sufficiently large number of seeds in each configuration and averaged over many configurations to obtain the probability distribution. (b) Schematic of cluster orientation estimation in a silo. Here the seeds are contacts with wall particles (black) within a vertical strip Δz , and the angle θ_i with respect to the horizontal (in the clockwise direction) between the line connecting a particle i in a cluster (green) and the wall particle is measured.

E. Radius of gyration and size of subnetworks

To study the size of clusters of different linearity, we computed their radius of gyration R_g as a function of r . For a cluster of linearity r , the radius of gyration is

$$R_g = \sqrt{\frac{1}{N_c} \sum_{i=1}^{N_c} (\mathbf{x}_i - \mathbf{x}_{\text{cm}})^2} \quad (\text{S13})$$

where N_c is the number of particles in the cluster, \mathbf{x}_i is the position vector of particle i and \mathbf{x}_{cm} is the position vector of the centre of mass of the cluster; this is then averaged over all non-percolating clusters of linearity r . Figure S2.4(a) shows R_g as a function of linearity r for 2D isotropic compression ($N_T = 12,500$, $L = 100d_p$). The choice of seeds does not have a significant influence on R_g , unlike the mean force in the cluster (Fig. 3a). The number of particles $N(r)$ in clusters of linearity r is shown in Fig. S2.4(b), wherein it is clear that the occurrence of clusters of linearity greater than r_c , and therefore large R_g , is negligibly small.

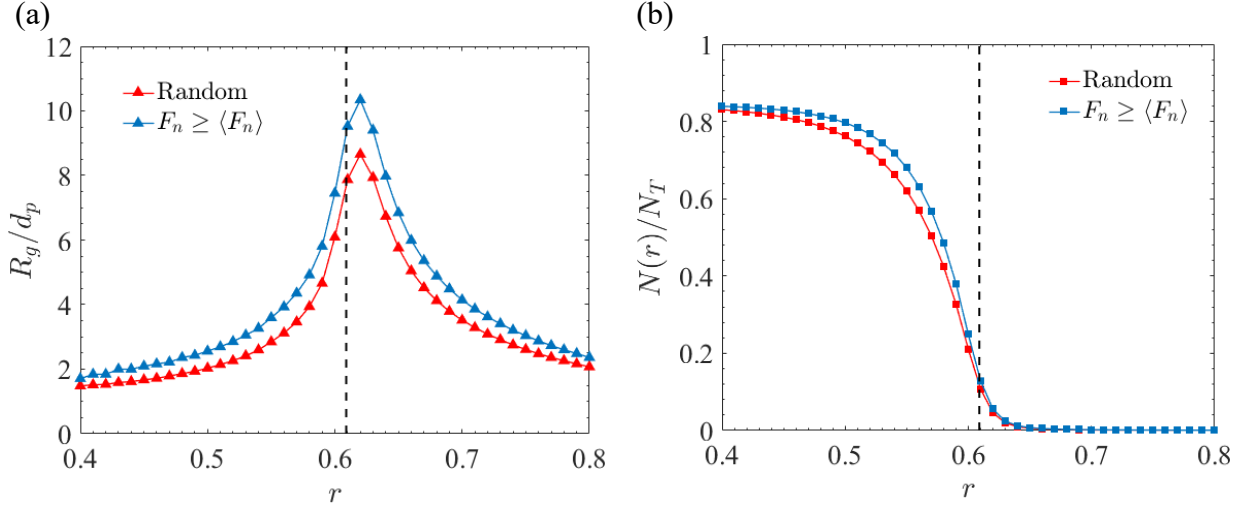


FIG. S2.4. (a) Radius of gyration R_g of non-percolating clusters. (b) Number of particles $N(r)$ in clusters of linearity r scaled by the total number of particles N_T . The results are for 2D isotropic compression with dimensions $100d_p \times 100d_p$, area fraction of 0.8132, averaged over 200 independent configurations. The dashed line marks the value of r_c , which here is 0.609.

III. Creation of static and sheared configurations

A. Isotropic compression

To generate the configurations, we start from an initial random configuration of non-overlapping spheres in a 2D square box, whose walls are composed of array of spheres of mean diameter d_p . In the initial state, the area fraction is 0.1 and the minimum distance between any two particles is $1.5d_p$. From the initial state, a force F is applied on the walls, which is increased linearly with time from zero to F_{\max} in a period of $940\sqrt{d_p/g}$, after which the simulations are continued at force F_{\max} until the kinetic energy per particle in the system decays to $\approx 10^{-11}m_pgd_p$. This process is repeated to create multiple configurations. The results for isotropic compression shown in Fig. 2 are for an applied stress of $\sigma \equiv F_{\max}/(Ld_p) = 2.45 m_p g/d_p^2$ and area fraction is 0.8132; decreasing or increasing σ causes a corresponding change in the critical linearity r_c [Fig. S3.1(c)]. The results shown in Fig. 2(a), 2(b) are averages over 2000 configurations, and in Fig. 3(a), 3(b) over 200 configurations.

B. Uniaxial compression

The initial loose packed configuration and the final compressed configurations are obtained in the same manner as in isotropic compression, with the sole difference that the left and right boundaries are periodic. The x dimension of the rectangular box is fixed at $L_x = 100d_p$ [Fig. S3.1(b)], and the y dimension L_y , bounded by the rigid walls, is varied to reach the desired initial state. From the initial loose state, a total force F is applied on the two walls, which is

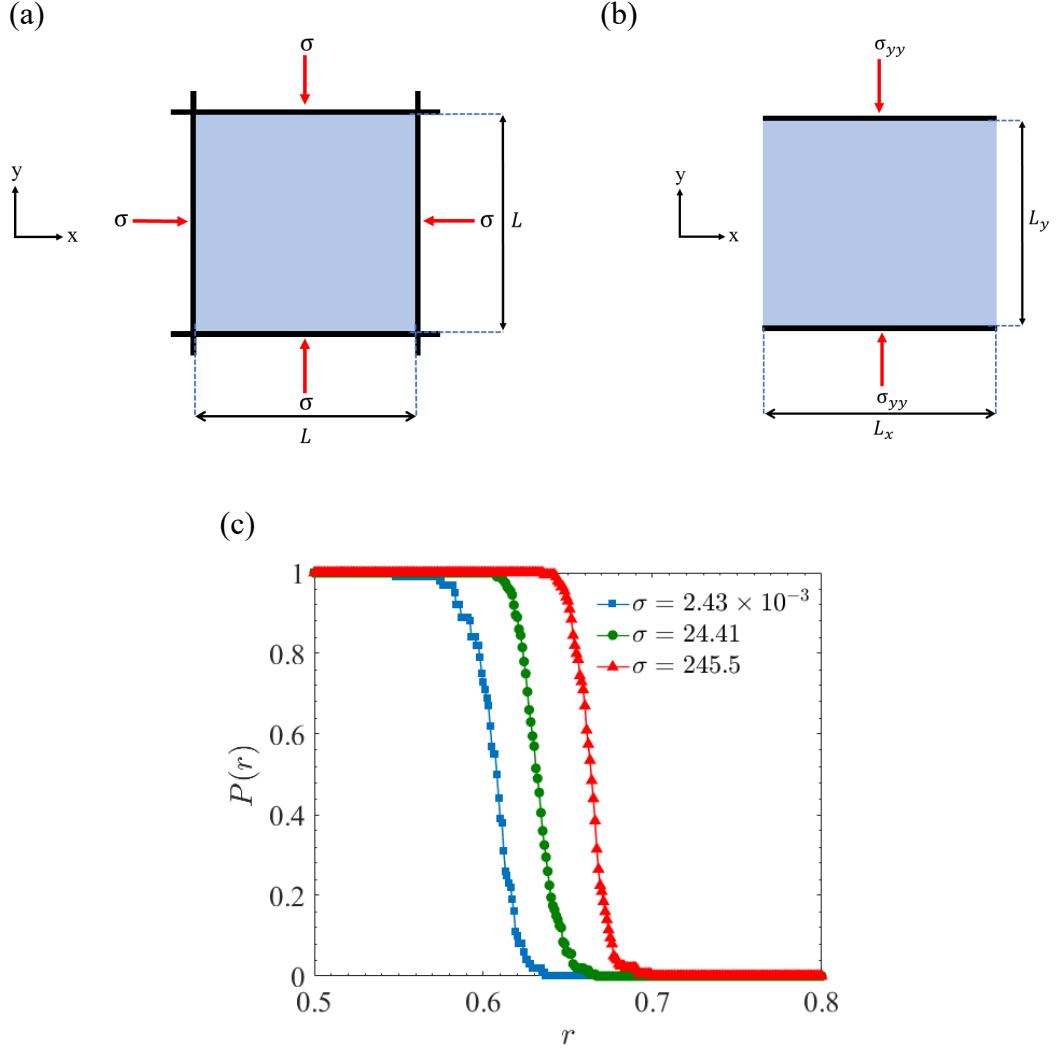


FIG. S3.1. (a) Schematic of 2D isotropic compression. (b) Schematic of 2D uniaxial compression. The left and right boundaries are periodic. (c) Linearity percolation in 2D isotropic compression for increasing boundary stress σ (in units of $m_p g/d_p^2$). The area fractions (and coordination numbers, excluding rattlers) of the systems in the order of increasing σ are 0.811 (3.10), 0.817 (3.32) and 0.827 (3.62) respectively. The results shown are averages over 200 configurations. Rattlers are particles with one or no contact.

increased linearly with time from zero to F_{\max} in a period of $940\sqrt{d_p/g}$, after which the simulations are continued with constant force F_{\max} until the kinetic energy per particle in the system reaches $\approx 10^{-11}m_p g d_p$. For the uniaxial system shown in Fig. 2(c) and 4(b), $\sigma \equiv F_{\max}/(L d_p) = 0.75 m_p g/d_p^2$. In the nearly static final state, the y dimension $L_y \approx 100 d_p$, and area fraction is 0.811. The results in Fig. 2(c) are averages over 300 configurations for all the geometries and forcing.

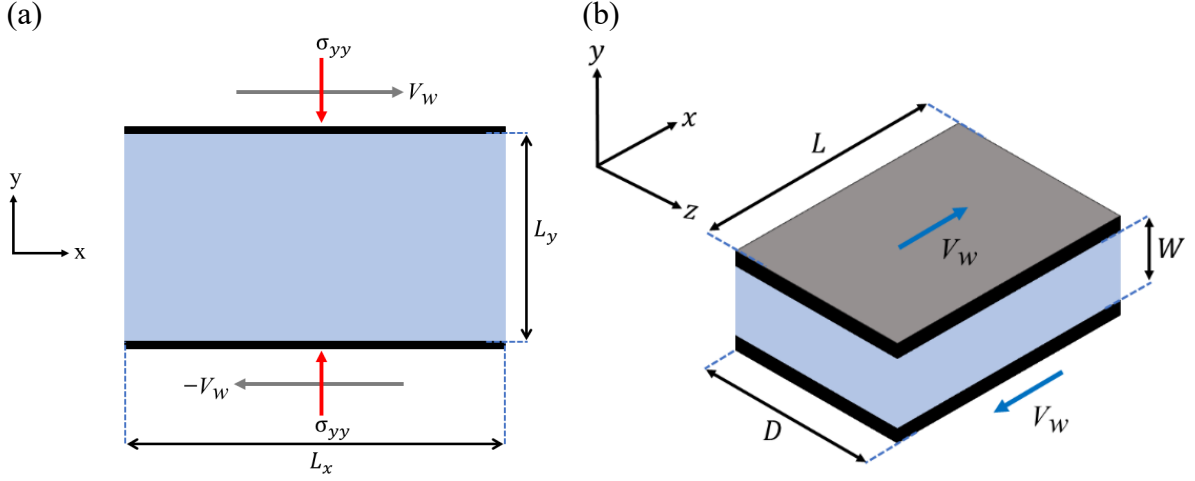


FIG. S3.2. Schematic of plane shear in (a) 2D and (b) 3D.

C. Plane shear

In 2D plane shear a monolayer of particles was sheared by restricting their centres from moving out of the x - y plane, with periodic boundaries in the x direction [Fig. S3.2(a)]. The simulations were started from an initial loose configuration generated in the same manner as in uniaxial compression; thereafter, in addition to applying compressive forces on the two walls, the walls were translated at velocities V_w and $-V_w$ in the x direction. The normal force was increased linearly from zero to F_{\max} in a time of $1880\sqrt{d_p/g}$, after which the simulations were continued with constant force and wall velocity for strain $\gamma \approx 30$; the total kinetic energy of the system reaches a steady state value after $\gamma \approx 10$. At steady state, the dimensions of the system are $L_x = 100d_p$, $L_y \approx 100.5d_p$, area fraction is 0.8133, and normal stress is $\sigma_{yy} \equiv F/(L_x d_p) = 0.75 m_p g/d_p^2$.

The configurations for 3D shear were created in the same manner, but allowing the particles to translate and rotate in all 3 directions. Periodic boundaries are imposed in the x and z directions [Fig. S3.2(b)]. While the 2D shear simulations were performed at constant normal stress σ_{yy} , the 3D shear simulations were performed at constant volume – the compression of the loose configuration was stopped upon reaching a volume fraction ϕ of 0.595, after which the z -coordinates of the walls were fixed, and shearing was commenced by moving the top and bottom walls at constant velocities of V_w and $-V_w$, respectively. The steady state properties were determined after shearing for a strain of $\gamma \approx 100$. The dimensions of the system at steady sheared state are $L = 30d_p$, $D = 20d_p$, $W = 21d_p$.

The regime of flow is characterized by the Savage number [R8], defined as the ratio of stress due to grain inertia to the total stress,

$$Sa = \frac{\rho_p d_p^2 \dot{\gamma}^2}{\sigma_{yy}} \quad (\text{S14})$$

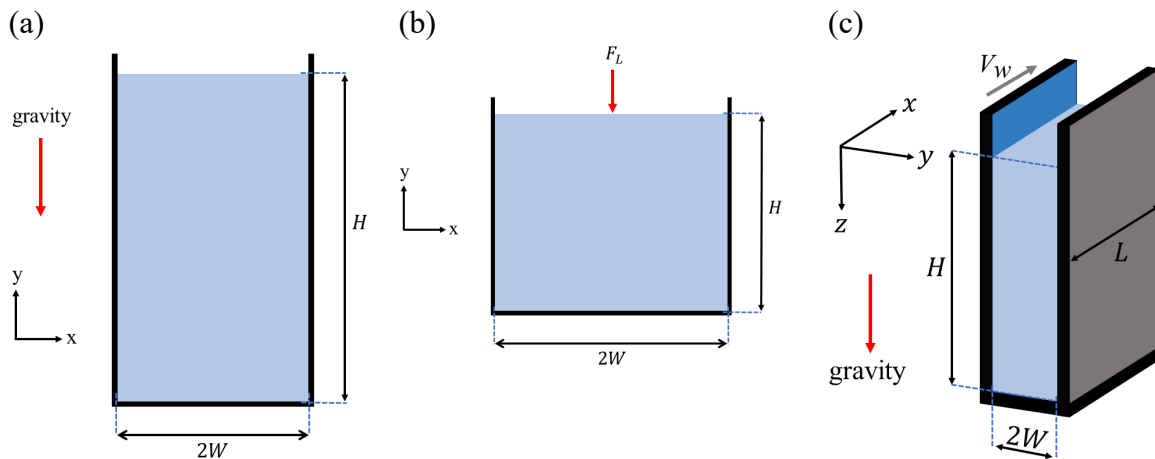


FIG. S3.3. Schematics of the silo and the 2D point force simulations. (a) 2D silo. (b) Point force acting at the symmetry axis on the free surface of the 2D silo. (c) 3D silo; the wall velocity V_w is zero in the static case.

where ρ_p is the intrinsic density of the particles and $\dot{\gamma}$ is the shear rate. The inertia number I used in many recent studies is $Sa^{1/2}$. The Savage number for 2D shear flow is $\approx 10^{-8}$, thereby implying that granular material is in the slow flow, or quasistatic, flow regime. The Savage number for 3D shear flow is $\approx 10^{-4}$, at which effects of grain inertia are expected to be small but finite – however, the qualitative features of the contact network are found to be the same as for lower Sa .

D. Silo and point force simulations

For all the studies pertaining to the analysis of linearity percolation and contact force statistics in silos [Figs 2(c) and 4(e), 4(f)], a vertical container of rectangular cross section was filled by ‘raining’ the grains into it from above under the influence of gravity. The walls were constructed of particles of diameter d_p in exactly the same manner as in the 2D and 3D systems described above. To fill a silo of dimensions $L \times 2W \times H$, particles were created randomly in a pouring region placed above the silo to a volume fraction of 0.01, and allowed to fall into the silo under the influence of gravity. The dimensions of the pouring region were $(L - d_p) \times (2W - d_p) \times H_r$, where H_r was typically between $H/2$ and $H/3$, and its base was $5-10d_p$ above the free surface of silo (Fig. S3.3). The creation of particles in the pouring region and their raining was continued until the container was filled to the required fill height. To achieve a static state, the simulations were continued until the kinetic energy per particle reduced to $10^{-12} m_p g d_p$. This process was repeated to create multiple configurations. The dimensions of the 2D silo are $2W = 40d_p$, $H = 490d_p$ [Fig. S3.3(a)], and the particles centres are constrained from moving out of the in the x - y plane. The dimensions of the 3D silo are $2W = 20d_p$, $L = 25d_p$, $H = 265d_p$ [Fig. S3.3(c)], with periodic boundaries in the x direction.

For the point force simulation [Fig. S3.3(b)], a static 2D bed of dimensions $2W = 100d_p$, $H = 50d_p$ was first created, and a point force $F_L = m_p g$ was applied to the particle closest to the midpoint on the free surface; the particle positions and forces were further evolved till the kinetic energy per particle reduced to $10^{-12}m_p g d_p$. The response to the point force was measured by determining the change in the force ΔF_n at each contact upon application of the point force. Due to plastic rearrangements, the normal forces either reduce or vanish in a small fraction of contacts; for our analysis, only the contacts for which $\Delta F_n > 0$ were considered. The network statistics shown in Fig. 3(c) was obtained from 2000 configurations.

For the analysis of the force network in a sheared column [Fig. 4(f)], static configurations were first created in the same manner as that of a static 3D silo, discussed above. Subsequently the column was sheared, by moving the left wall [Fig. S3.3(c)] with constant velocity V_w in the x direction, for strain $\gamma \approx 50$. The bed dilates during shear, and its steady state dimensions were $2W = 20d_p$, $D = 25d_p$, $H = 275d_p$. The vertical shear stress on the wall σ_{yz} and cluster angles θ were then obtained by averaging over the steady state configurations. The shear stress σ_{yz} is given by

$$\sigma_{yz} = \frac{\sum_i F_z^i}{L \Delta z}, \quad (\text{S15})$$

where Δz is the width of the segment of the wall at height z , and F_z^i is the vertical component of the force transmitted to the wall particle i in the segment. We chose $\Delta z \approx 11d_p$ to determine the variation of σ_{yz} with depth z [Fig. 4(e), 4(f)]. In the sheared column, the axial stress was measured along the stationary wall.

IV. Random geometric graphs (RGG)

Random geometric graphs are random graphs embedded in Euclidean space [31,32]. RGGs are used to model spatial networks and in studies of continuum percolation [31,32]. We generate random graphs on a 2D square domain of dimension L . The positions of N points in the domain are randomly generated, and any two points are considered connected if they are separated by a distance $\leq R$, where R is referred to as the connection distance. The average number of connections per point $\langle k \rangle$ in 2D is given by [31,32],

$$\langle k \rangle = \rho \pi R^2 \quad (\text{S16})$$

where ρ is the number density of points. The number of points to be generated is found using the values of ρ , and area of the domain, A . The value of ρ used in this study is 0.6363, and R was chosen such that the average coordination number (number of connections per point) $\langle k \rangle$ is 6. In this graph the points are the nodes and the connections are the edges. The percolation probability and finite size scaling analysis of RGG is shown in Fig. S4. Our estimate of critical linearity for the RGG is 0.646 ± 0.0009 .

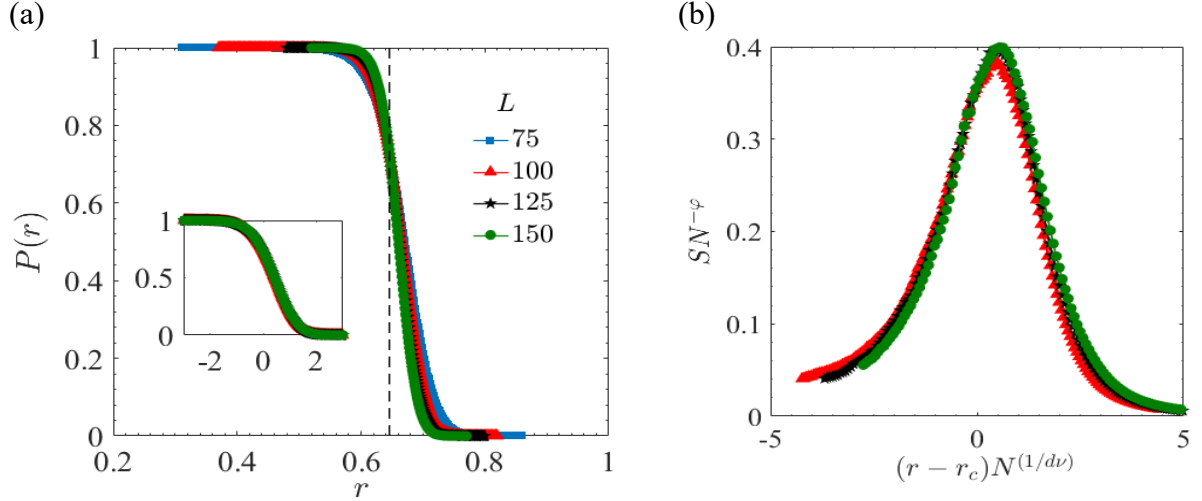


FIG. S4. Finite size scaling in random geometric graphs (RGG). The system size L is in units of the connection distance R . (a) Percolation probability for different system sizes; the inset shows collapse of all the data when $P(r)$ is plotted against $(r - r_c) N^{1/dv}$ (see Fig. 2). (b) Finite size scaling of the mean cluster size $S(r)$. The results are obtained from 50000 configurations.

V. Effect of grain interaction parameters on linearity percolation

The influence of the interaction parameters was studied by varying the friction coefficient μ and the spring stiffness k_n in equations (S5) and (S6). The results are shown in Fig. S5, where the occurrence of linearity percolation transition for all values of the parameters is apparent. The value of r_c decreases as μ increases, or k_n decreases. In both cases, r_c varies monotonically with the coordination number.

The purpose of Figs S3.1 and S5 is to show that linearity percolation is robust and exists for a wide range of pressure and particle interaction parameters. While the figures show a trend in the dependence of r_c on σ , μ and k_n , the precise values of r_c for different values of the parameters has not been determined, as that requires a finite size scaling analysis which is computationally intensive.

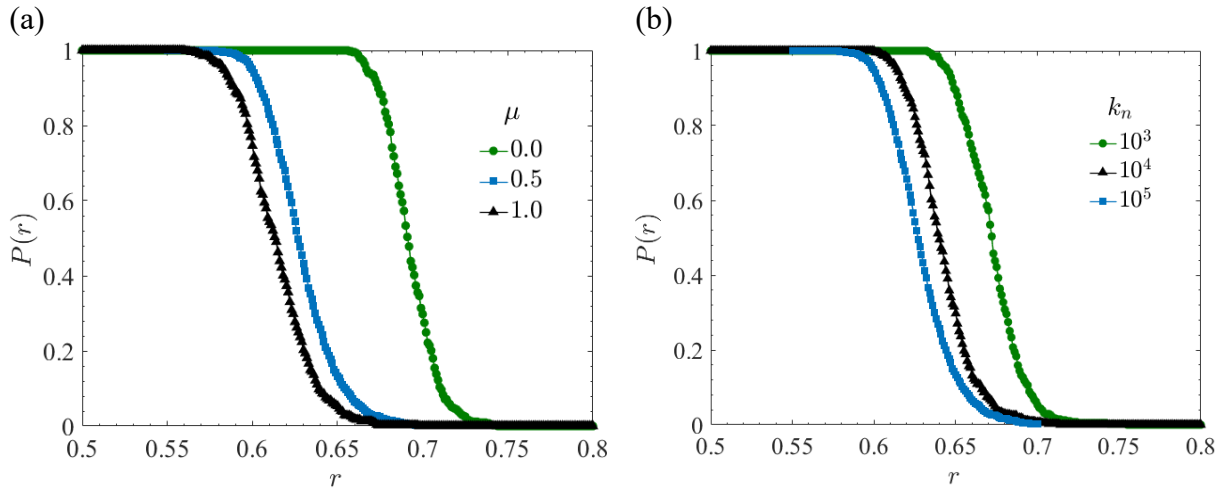


FIG. S5. Variation of the percolation probability with r for different values of (a) the friction coefficient μ , and (b) the particle stiffness k_n . The data shown are for isotropic compression system with dimensions $50d_p \times 50d_p$ ($L_x \times L_y$). The value of γ_n in (a) was adjusted to keep the normal coefficient of restitution at 0.7 – all other interaction parameters are as described in Fig. S1. The results shown are averages over 500 independent configurations.

Supplemental References

- [R1] P. A. Cundall, and O. D. Strack, *Geotechnique* **29**, 47 (1979).
- [R2] S. Plimpton, *J. Comp. Phys.* **117**, 1-19 (1995).
- [R3] L. E. Silbert, D. Ertas, G. S. Grest, T. C. Halsey, D. Levine, and S. J. Plimpton, *Phys. Rev. E* **64**, 051302 (2001).
- [R4] T. H. Cormen, C. E. Leiserson, R. L. Rivest, and C. Stein, *Introduction to Algorithms* (MIT press, Cambridge, 2009).
- [R5] R. Sedgewick, and K. Wayne, *Algorithms* (Addison-Wesley Professional, Upper Saddle River, 2011).
- [R6] M. D. Rintoul, and S. Torquato, *J. Phys. A* **30**, L585 (1997).
- [R7] E. W. Dijkstra, *Numer. Math.* **1**, 269 (1959).
- [R8] S. B. Savage, and K. Hutter, *J. Fluid Mech.* **199**, 177-215 (1989).